POLITECNICO DI TORINO
Repository ISTITUZIONALE

Comparative assessment of gas and water atomized powders for additive manufacturing of 316 L stainless steel: Microstructure, mechanical properties, and corrosion resistance

Original
Comparative assessment of gas and water atomized powders for additive manufacturing of 316 L stainless steel: Microstructure, mechanical properties, and corrosion resistance / Jandaghi, M.R., Pouraliakbar, H., Iannucci, L., Fallah, V., Pavese, M.. - In: MATERIALS CHARACTERIZATION. - ISSN 1044-5803. - ELETTRONICO. - 204:(2023). [10.1016/j.matchar.2023.113204]

Availability:
This version is available at: 11583/2982412 since: 2023-11-10T13:24:48Z

Publisher:
Elsevier Inc.

Published
DOI:10.1016/j.matchar.2023.113204

Terms of use:

This article is made available under terms and conditions as specified in the corresponding bibliographic description in the repository

Publisher copyright
Elsevier postprint/Author's Accepted Manuscript

© 2023. This manuscript version is made available under the CC-BY-NC-ND 4.0 license http://creativecommons.org/licenses/by-nc-nd/4.0/.The final authenticated version is available online at: http://dx.doi.org/10.1016/j.matchar.2023.113204

(Article begins on next page)

24 June 2026

Manuscript File Click here to view linked References

Comparative Assessment of Gas and Water Atomized Powders for Additive Manufacturing of 316L stainless steel: Microstructure, Mechanical properties, and Corrosion Resistance

Mohammad Reza Jandaghi [*,1], Hesam Pouraliakbar [2], Leonardo Iannucci [1], Vahid Fallah [2], Matteo Pavese [1]

[1] *Department of Applied Science and Technology, Politecnico di Torino, Corso Duca Degli Abruzzi 24, 10129 Torino, Italy*

[2] *Azar Advanced Manufacturing Laboratory (AAML), Department of Mechanical and Materials Engineering, Queen's University, Kingston, ON K7L 3N6, Canada*

Corresponding author**; E-mail: **mohammadreza.jandaghi@polito.it

Abstract

In this study, the microstructure, and mechanical properties of 316L stainless steel (SS316L) produced by laser powder bed fusion (LPBF) using water-atomized (WA) and gas-atomized (GA) powders were compared. The results showed that the use of WA powder, with a finer average particle size and better spreadability, led to significantly higher values of tensile strength (UTS), yield strength (YS), elongation (El%), and toughness in the WA samples (728 MPa, 580 MPa, 31.8%, and 215 J/m^3, respectively) compared to the GA sample (602 MPa, 503 MPa, 25.2%, 145 J/m^3, respectively). The WA samples also exhibited a non-uniform hardness distribution and superior work-hardening rate due to the presence of multiple inclusions that tightly bound to the matrix and created stress fields, increasing the required energy for dislocation motion. The higher solidification rate of melt pools in the WA sample left more intensive residual stress with distorted grains, exhibiting a higher grain orientation spread (GOS). Additionally, a multitude of geometrically necessary dislocations (GNDs) formed around the boundaries of elongated grains with tilted boundaries to maintain lattice continuity, resulting in a higher kernel average misorientation (KAM) and congestion of low-angle grain boundaries (LAGBs), particularly in the WA sample. XRD patterns confirmed the higher lattice distortion in the WA sample, and the smaller cellular structures observed in SEM images were consistent with the higher dislocation density observed in the WA specimens. Finally, the WA sample exhibited lower surface roughness and rather higher resistance to corrosive media containing chlorides.

Keywords: *Additive Manufacturing, Water Atomized; Electron Back Scatter Diffraction (EBSD); Cellular structure; Geometrically Necessary Dislocations (GNDs).*

1. Introduction

In recent years, additive manufacturing (AM) technologies have growingly been replacing traditional production methods [1]. Although additive manufacturing (AM) methods were initially utilized for prototyping purposes, they have now become the predominant production technique for numerous critical components within the automotive and aerospace industries [2]. The Laser Powder Bed Fusion (LPBF) is one of the AM methods for manufacturing complex-shaped components using a laser source according to computer-aided design (CAD) data [3]. In the powder-bed systems, a re-coater carries the powder from a feedstock chamber and spreads it on the build plate [4]. To identify an ideal metallic powder for AM, its features, such as average particle size, particle size distribution, surface area, flowability, apparent density, tap density, moisture content, and trapped porosity, need to be documented [5]. Spreadability plays a crucial role in printing faultless and dense components, and a powder with proper size distribution composed of particles with a spherical shape and smooth surface is known as the ideal feedstock for AM [6, 7]. This is because small friction coefficient between the spherical powders facilitates their spreading [8]. There are three prevalent processes for fabricating proper powders for AM, including "plasma atomization," "gas atomization," and "water atomization" [9]. Among them, plasma atomization provides the most spherical shaped powders. Gas atomization produces spherical powders with appropriate morphology at a lower price than plasma atomization [10]. Nonetheless, the simplest and cheapest atomization method is water atomization [11]. Due to the high cooling rate in water atomization, the particles acquire an irregular shape [12]. In contrast, the inert atmosphere of the chamber in gas atomization reduces the solidification rate of the particles and creates a more regular morphology in the final powder [13]. Moreover, the oxygen content of the WA particles is higher than in gas and plasma atomized particles. Oxygen uptake and chemical oxidation during AM directly arise from high oxygen content in the feedstock powder, which not only affects the powder flow but also degrades the mechanical properties of the printed parts [14]. So far, WA powders of different alloys such as Al [15], Zn [16], Ti [17], IN625 [18], IN738 [19], NiTi [13] and high entropy alloys (HEAs) [20] have been evaluated for AM applications. However, due to the oxygen pickup, water atomization is not an appropriate production route for Al, Ti, and alloys containing such reactive elements, and the most suitable material for water atomizing is steel [21]. On the other hand, using WA powder

instead of GA can reduce the production cost by a large factor, i.e., ~10-80% [22]. To overcome the drawbacks of WA powders, some solutions have been proposed. Schade et. al [5] designed a multi-step process to eliminate the more irregular particles of WA iron powder. Despite increasing the apparent density and flowability of the powders, wasting about 50% of the initial powder in the separation line reduced the cost-efficiency of this process. Boisvert et. al inoculated magnesium into the melt of SS304 before the atomization to favor the direct formation of more spherical powders with fewer internal pores [6]. Chikosha et al. [23] and Park et al. [24] employed an inductively coupled thermal plasma system for spheroidizing irregular powders. Consequently, the fine particles were majorly removed and the flowability of the powder significantly improved. Mirzababaei et al. suggested adding a solid lubricant such as zinc stearate to the feedstock to reduce interparticle friction and enhance flowability [25]. Calculating the Hausner ratio (tap density/apparent density) is the simplest way to predict the flowability of the powders. Generally, the Hausner ratio and avalanche angle of WA powders are lower than GA ones [26]. Howbeit, beyond a threshold, amelioration of the Hausner ratio and sphericity cannot majorly affect the final part density [27]. Nonetheless, some authors declared that the bulk densification of the printed parts with WA powder was close to those built by the GA counterparts even by using the same process parameters [28, 29]. Compared to GA powders, irregular WA particles have a rougher surface with a higher surface area to volume ratio and benefit from higher laser absorption and lower reflectivity [30, 31]. Thus, applying similar energy densities would provide higher heat input for melting the WA powder [32].

Previous studies have demonstrated that GA powders can yield components with greater densification and mechanical strength at lower energy densities while maintaining similar particle sizes. However, when higher energy densities are employed, WA powders can achieve comparable densities and mechanical properties to GA powders [33]. SS316L is a widely used alloy due to its exceptional corrosion resistance and mechanical properties [34, 35]. Optimizing the process parameters of the LPBF method can lead to significant similarities in the parts produced using WA and GA SS316L powders. [36]. In the current study, the authors demonstrated that reducing the average particle size of WA powder, which has higher laser absorption and oxide-forming elements, would enhance its

flowability and result in higher mechanical properties compared to GA samples. Therefore, the morphology, chemical composition, and structure of the feedstock powders and printed samples for both WA and GA were analyzed and compared to the mechanical behavior and corrosion resistance of the final products.

2. Materials and processing

GA and WA powders of SS316L used in the current study were provided by Höganäs AB and Pometon S.p.A (Italy), respectively. Both samples were printed by a Concept Laser Mlab Cusing with a laser spot size of 50 µm and a laser power of 95 W, scanning speed of 500 mm/s, layer thickness of 25 µm, hatching distance of 74 µm, and rotation angle of 67° as the optimum parameters. Tensile dog-bone samples were printed perpendicular to the building direction according to the E8 standard with gauge dimensions of 32×6×4 mm^3.

2.1. Characterization

The powders and printed samples were mechanically polished with the SiC papers (up to 4000 size) and mirror polished by Largo 9, Dur 3, NAP B1 and OP-S NonDry, subsequently. The microscopy characterization performed using an Olympus DXS1000 digital optical microscope, a Leica DMI5000M microscope, a JEOL JSM7001F FE-SEM and a HITACHI SU-70 FEGSEM equipped with an EBSD (EDAX-Hikari Plus) detector. The EBSD data were analyzed by the EDAX OIM Analysis™ (TSL) software and MATLAB™ toolbox MTEX 5.9.0. Lattice parameters were measured through X-ray diffraction (XRD) using an X-Pert Philips diffractometer. The tensile test was performed by a Zwick/Roell Z050 testing machine at the strain rate of 2×10^{-3} S^{-1}. The microhardness measurement was carried out with a Leica VMHT machine and applied load of 0.1 kg for a dwell time of 15 s. The Laboratory Equipment Corporation (LECO) analysis with ONH836 analyzer was employed to measure the concentrations of oxygen, nitrogen, and hydrogen in the fabricated parts through LPBF.

2.2. Corrosion resistance

All electrochemical measurements were performed in 3.5 wt% NaCl solution after mounting the samples in epoxy resin and polishing them to a mirror-like finish. Based on a wire diameter of 0.5 mm and an immersed length of 70 mm, the counter electrode had an approximate area of 1.1 cm^2, while the exposed area was 0.9 cm^2. All the results presented in this study were normalized with respect to this specific area. A 3-electrode

electrochemical cell was used for the measurements, with the sample as the working electrode, a platinum wire as the counter electrode, and an Ag/AgCl electrode as the reference. The corrosion tests were carried out at room temperature, using the Ivium-n-Stat potentiostat. Prior to each measurement, the Open Circuit Potential (OCP) of the sample was measured for 30 minutes. For Cyclic-Potentiodynamic Polarization (CPP) measurements, the potential was scanned from -0.2 V vs OCP towards anodic voltage values at a scan rate of 10 mV/min with potential steps of 1 mV. The scan direction was reversed when the measured anodic current density was equal to 1 mA/cm^2, and the measurement ended at -0.2 V vs OCP. Electrochemical Impedance Spectroscopy (EIS) was performed by applying a sinusoidal stimulus of 10 mV around the OCP. The measurements were carried out in the frequency range of 10-2 Hz to 105 Hz, acquiring 10 points per frequency decade. Each electrochemical measurement was repeated three times.

3. Results and discussions

3.1. Powder analysis

The morphology and size distribution of the powders obtained by gas and water atomization were evaluated using a digital optical microscope and SEM analysis (**Fig. 1(a, b)**). Comparative analysis of the circular diameter (**Fig. 1(c, d)**) and circularity (**Fig. 1(e, f)**) of the powders revealed that WA powder has a finer particle size with lower circularity. In the context of the particles used in additive manufacturing, "circularity" refers to a geometric property that characterizes the shape of the particle. It specifically quantifies the degree to which the particle deviates from a perfect circle. Measuring the circularity of particles would aid to assess their sphericity and evaluate the quality and uniformity of the particles used in additive manufacturing processes. The irregular shape of WA particles is attributed to the rapid solidification of molten droplets during the atomization process. In the WA process, molten metal is subjected to high-pressure water jets that break it into droplets. These droplets cool down rapidly, preventing them from forming a spherical shape and instead freezing into a non-spherical shape with a high aspect ratio. The high surface tension of the water and the high cooling rate prevent the droplets from attaining a spherical shape, resulting in an irregular particle shape. This shape can be advantageous in improving the packing density of the powder, leading to better powder flow and higher

build density during additive manufacturing processes. However, it can also pose challenges in powder handling and flowability. In contrast, gas atomization produces more uniform cooling rates and spherical-shaped particles by atomizing molten metal with a high-velocity gas stream. This process allows for greater control over cooling rate, with the surface tension of the molten metal pulling it into a spherical shape as it cools. Previous studies have shown that particle size strongly influences flowability, with finer particles exhibiting lower spreadability [32]. The average circular diameter of GA and WA powders was 29 µm and 22 µm, respectively, which falls within the optimal particle size distribution range for LPBF (10-45 µm) [6].

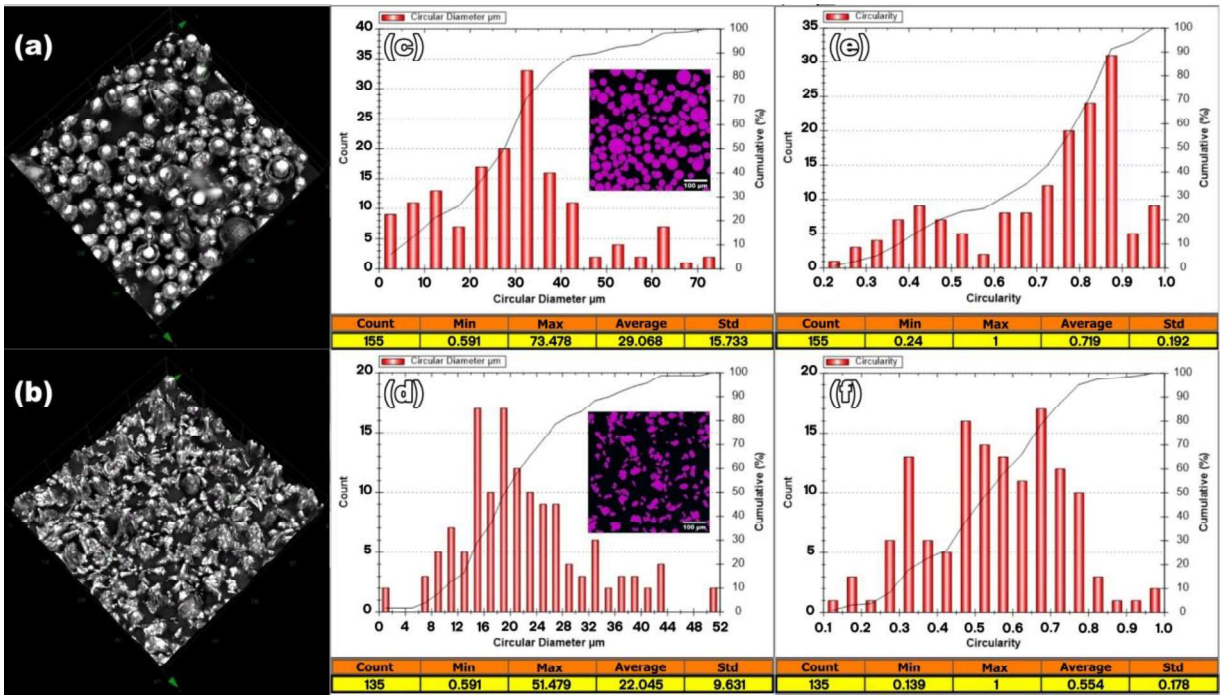

Fig. 1: Optical 3D micrographs and distribution histograms of the circular diameter and circularity of GA (a, c and e) and WA (b, d and e) samples.

Reducing the particle size range of WA powder has been shown to enhance its flowability. This is because smaller particles have a greater surface area-to-volume ratio, which makes them more prone to agglomeration and interparticle forces, such as van der Waals forces, causing them to stick together and form clusters. Such agglomeration can raise the bulk density of the powder and decrease its flowability. To counteract these effects, reducing the particle size range of the powder helps to mitigate agglomeration and interparticle forces, yielding a more uniform powder with better flowability. Smaller particles can also

fill the gaps between larger particles, which further improves the packing density and flowability of the powder. For industrial applications, selecting an appropriate layer thickness is critical to productivity. Typically, the optimum layer thickness that ensures a smooth powder bed, maximum compactness, and proper bonding between successive layers in AM fabricated samples is between D(50) and D(90) of the powder feedstock **[28]**. In this study, both GA and WA samples were printed with a layer thickness of 25 µm. The particle size distribution of GA powder is wider than that of WA powder and can yield a higher packing density since the fine particles fill the voids between large adjacent particles **[10]**. Moreover, previous research has demonstrated that, in addition to powder morphology, the surface roughness of printed samples increases in proportion to powder flowability **[37]**.

The morphology and elemental distribution of the GA and WA powders were characterized by SEM imaging and elemental mapping, as shown in **Figs. 2(a)** and **2(b)**, respectively. The GA powder had a higher Mn content and lower Si content compared to the WA powder, a finding that was consistently observed across multiple powder particles. This trend has been reported previously for the same alloy **[38]**, as well as for 4130 **[39]** and 17-4 PH **[26]** steels. In addition, the WA powder had relatively large Si-rich inclusions, while the GA particles contained smaller Si-rich zones. The difference in Si content, combined with the higher oxygen content of the WA powder, could result in more inclusions in the WA sample during printing.

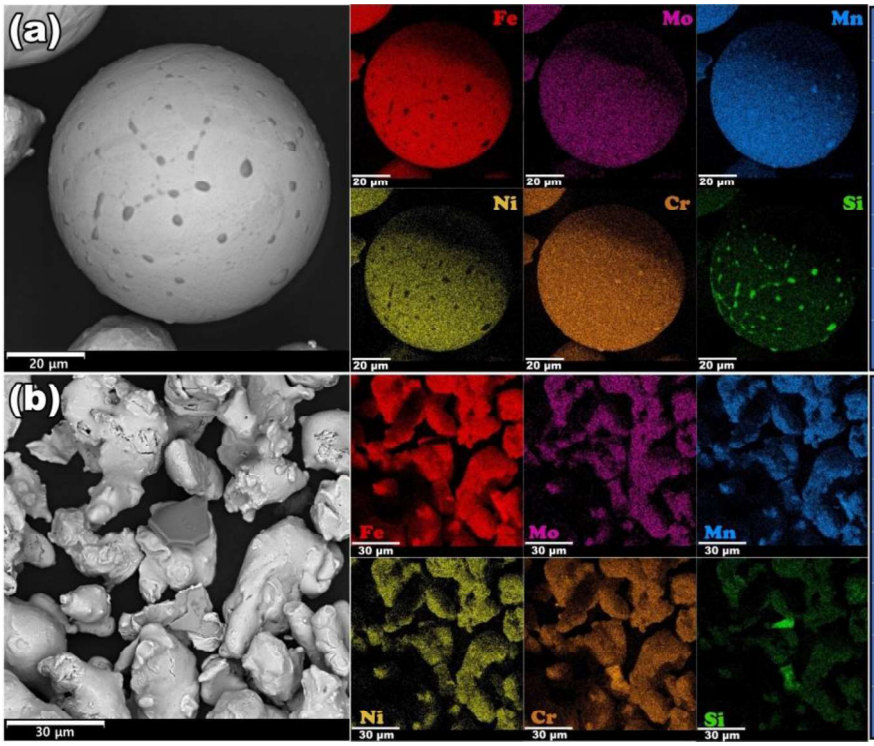

Element	At.%	Wt.%
Fe	62.07	62.24
Cr	20.73	19.36
Ni	11.40	12.01
Mn	2.71	2.67
Mo	1.77	3.06
Si	1.32	0.67

Element	At.%	Wt.%
Fe	65.00	65.92
Cr	19.63	18.53
Ni	10.31	10.99
Mn	0.17	0.17
Mo	1.53	2.66
Si	3.37	1.72

Fig. 2: SEM image and elemental distribution map analysis of GA (a) and WA (b) particles.

Fig. 3 presents the results of EBSD analysis for both GA and WA particles. The orientation maps in Figs. 3(a) and 3(b) show that both atomization methods produce polycrystalline particles. The phase maps in Figs. 3(c) and 3(d) reveal that ferritic and austenitic-ferritic particles (partially ferritic) were formed during water atomization of SS316L. The elemental distribution map of Fig. 3(e) shows that ferritic particles had a higher fraction of Fe and lower amounts of Ni, Cr, and Mo, and these particles are identified as δ-ferrite formed during the rapid solidification of the molten steel **[40]**. When liquid metal is sprayed into a water jet during water atomization, it causes rapid cooling and solidification of the droplets. This results in a high solidification rate, meaning that atoms have less time to diffuse and form their preferred crystal structure. For iron-based alloys, the high solidification rate in water atomization promotes the formation of a primarily ferritic microstructure since ferrite is the thermodynamically stable phase at high cooling rates. Gas atomization, on the other hand, usually results in a coarser microstructure with a mixture of ferrite and austenite phases. The chemical composition of the powder can also affect the phase evolution during solidification. In the case of the WA powder compared to GA powder, the lower Mn and higher Si content can promote the formation of ferrite since Si is a ferrite stabilizer and Mn is

an austenite stabilizer. Therefore, the combination of high solidification rate and chemical composition of the WA powder increases the chance of forming a primarily ferritic microstructure.

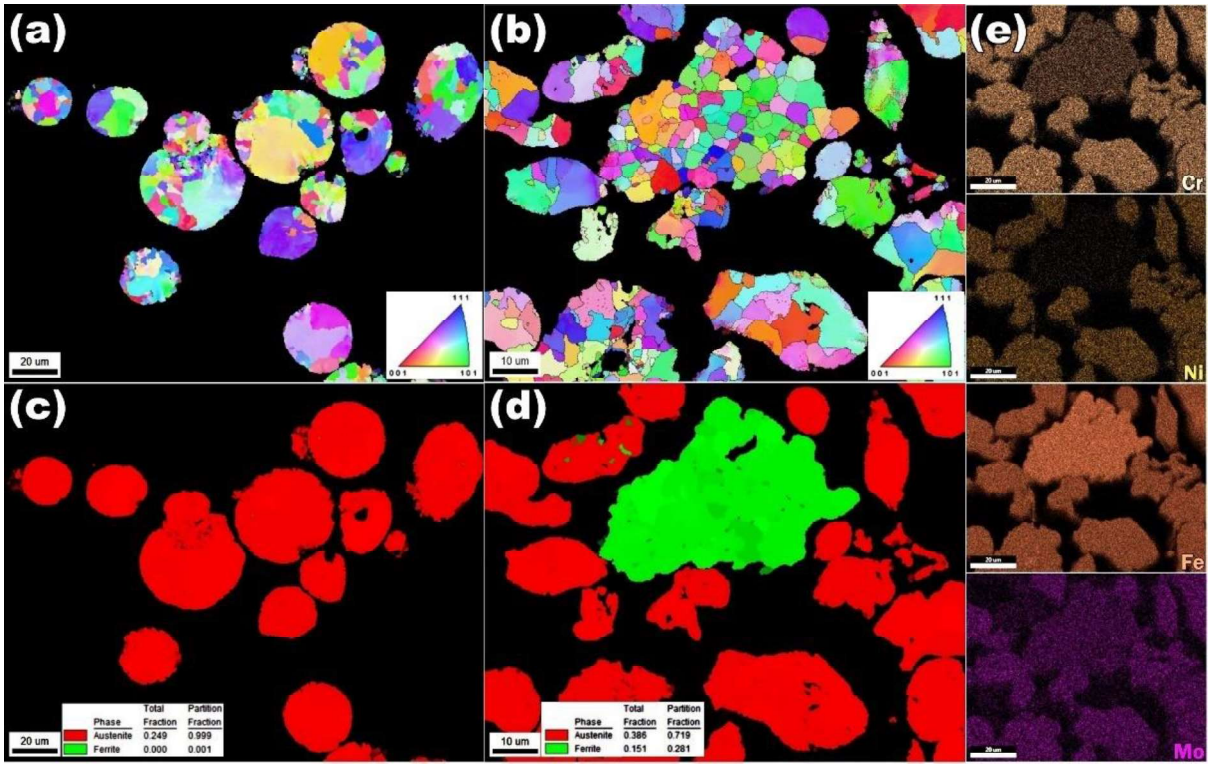

Fig. 3. EBSD orientation maps (a, b) and the corresponding phase maps (c, d) of GA and WA powders and elemental distribution map of the WA powder (e).

3.2. Microstructural characterization

Various analysis methods were used to compare the microstructure and lattice parameters of LPBF-fabricated samples using GA and WA powders. The results are presented in the following.

3.3. XRD

Figs. 4 present the XRD patterns of the GA and WA powders and the as-printed samples. As can be seen, the GA and WA powders both exhibit a peak of δ-ferrite (110) with a BCC structure at $2\theta = 44°$. However, the peak is more prominent in the WA powder than in the GA powder. This result is consistent with the fact that certain elements, including chromium, molybdenum, and silicon, tend to segregate during solidification, leading to

the formation of the ferritic phase. However, after printing the samples, the δ-ferrite peak disappeared. This can be attributed to either the complete dissolution of ferritic particles or a low concentration of ultra-fine ferritic phases that were not detected by the XRD analysis.

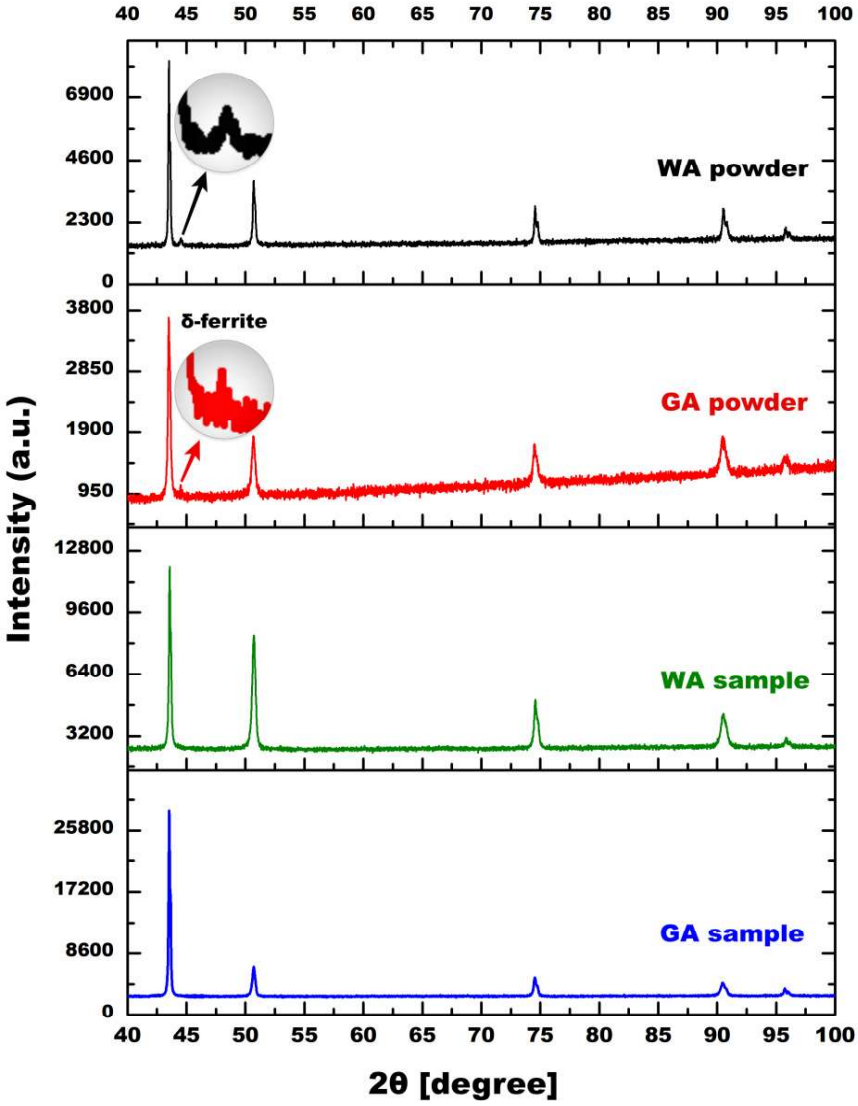

Fig. 4. XRD patterns of the GA and WA powders and as-printed samples.

Table 1 presents the lattice parameters of the GA and WA powders, as well as the as-printed samples. To determine the dislocation density of the samples, the Scherrer equation was used, which relates the peak broadening to the dislocation density, crystallite size, and the wavelength of the X-rays used in the measurement. The equation is expressed as:

$$\beta \cos\theta = K\lambda/D \quad (1)$$

where β is the full width at half maximum (FWHM) of the diffraction peak, θ is the diffraction angle, K is the Scherrer constant (typically taken as 0.9), λ is the wavelength of the X-rays, and D is the crystallite size. The crystallite size was obtained using the X'pert High score software, and the dislocation density (ρ) was calculated from the rearranged Scherrer equation:

$$\rho = (K\,\lambda)/(\beta \cos\theta\, D) \quad (2)$$

The results show that the WA specimen had a lower lattice constant of the austenite phase than its GA counterpart in both powder and printed samples. Additionally, the WA samples exhibited a smaller crystallite size and a higher dislocation density than the GA sample in the as-printed state. The lattice parameters of δ-ferrite in the WA and GA powders also showed a similar difference.

Table 1. Lattice parameters of the GA and WA powders and as-printed samples

XRD output	Phase	GA powder	WA powder	GA sample	WA sample
Lattice constant (Å)	ϒ-austenite	3.5992	3.5975	3.5986	3.5976
	δ-ferrite	2.8129	2.8772	-	-
Crystallite size (Å)	ϒ-austenite	351	626	474	408
	δ-ferrite	2209	378	-	-
Dislocation density (m^{-2})	ϒ-austenite	1.52E+13	3.14E+12	5.68E+12	7.53E+12
	δ-ferrite	2.05E+11	7.00E+12	-	-

The microstructure and lattice parameter differences between the GA and WA powders and printed samples can be explained by the varying cooling rates and solidification conditions during their production. Rapid solidification during water atomization results in a smaller crystallite size and a higher dislocation density in the WA sample, which can cause lattice distortion and a lower lattice constant. The lower lattice constant of the austenite phase in the WA sample suggests that its atoms are more closely packed together due to the smaller particle size and higher solidification rate of the WA powder. The formation of δ-ferrite is sensitive to cooling rate, and the higher solidification rate during water atomization may have favored the formation of δ-ferrite in the WA sample, leading to a lower lattice constant compared to the GA sample **[41, 42]**.

3.4. LECO test

Table 2. presents the results of measuring the amounts of oxygen, nitrogen, and hydrogen (ONH) in the as-printed samples produced using GA and WA powders. A higher oxygen and nitrogen content in the powder can result in the formation of oxide and nitride inclusions, respectively, during the solidification process. In addition, the higher hydrogen content in WA powder can lead to more porosity in the printed part. The printing chamber atmosphere for both GA and WA samples was similar (argon), indicating that the difference in ONH values should be attributed to the atomization media. The GA powder had a higher N value due to atomization in nitrogen inert gas, while the WA powder had higher O and H values due to atomization in water. Previous research has demonstrated that atomization in a nitrogen atmosphere can directly affect the chemical composition by stabilizing the austenite phase, as reported in literature **[21, 43]**. However, high nitrogen content could lead to solidification cracking **[44]**. In contrast, a higher oxygen content may adversely affect processing by disrupting layer adhesion, splitting the continuous laser track into multiple molten segments and spreading more inclusions **[45]**.

Table 2. The results of the LECO test

Material	Oxygen (%)	Nitrogen (%)	Hydrogen (ppm)
GA sample	0.0736 ± 0.0066	0.0633 ± 0.0012	39.6 ± 10
WA sample	0.185 ± 0.011	0.0222 ± 0.0005	95.4 ± 6.9

3.5. Microcopy investigation

Figs. 5(a) and **5(b)** display the optical microscope micrographs of the as-printed samples utilizing GA and WA powders, respectively. The micrographs clearly illustrate that the GA sample exhibits a fish-scale pattern grain structure, whereas the WA sample comprises columnar grains along the build direction (BD). The WA powder possesses smaller particle sizes and higher laser absorption, which enhances the bonding between deposited layers, consistent with prior investigations **[46]**. A high laser heat input results in deeper laser beam penetration, partial remelting of the last deposited layer, and strong grain orientations along the BD with nucleation taking place on the epitaxially grown grains. In comparison to the components produced with GA powder, those printed with the WA counterpart demonstrate superior surface finish, uniformity in deposition, and stronger

layer bonding [26]. The higher laser absorption of WA, in contrast to GA powder, creates hotter melt pools with a faster solidification rate, promoting a finer dendritic structure [47].

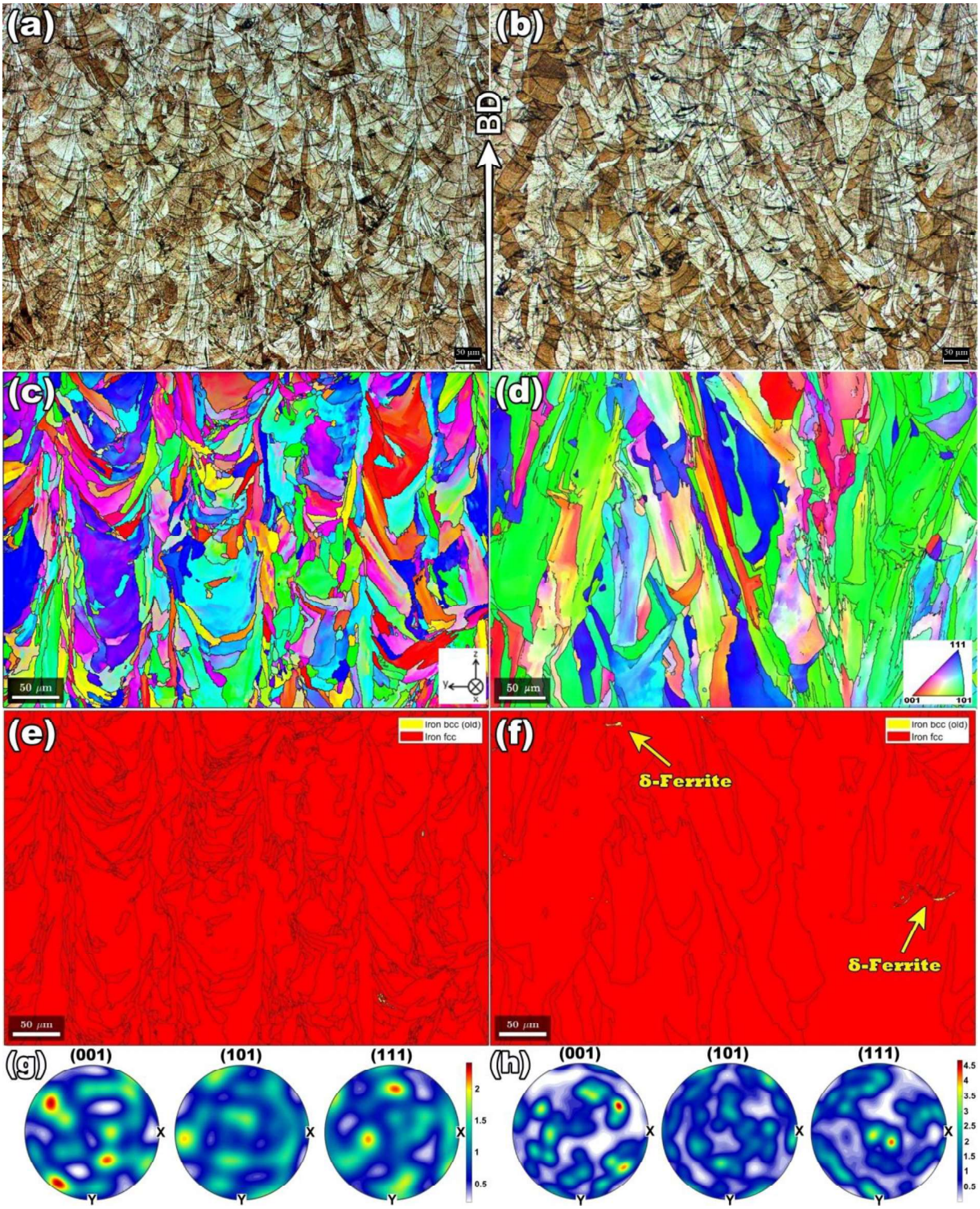

Fig. 5. OM micrograph (a, b), IPF color map (c, d), phase map (e,f) and PF (g, h) of GA and WA samples.

The IPF maps presented in **Figs. 5 (c, d)** illustrate the distinct differences in grain morphology between the GA and WA samples. As observed from the OM images, the WA sample exhibits more elongated grains along the BD. As already mentioned, WA powder with higher laser absorption would heat up faster upon exposure to laser energy, leading to more rapid melting and solidification. On the other hand, WA powder with lower laser absorption would take longer to heat up and solidify. The solidification rate is determined by the rate of heat transfer from the melt to the surrounding environment. As a result, the solidification front moves faster, leading to a higher solidification rate. Since the similar process parameters are applied for WA and GA powders with different particle sizes, the solidification rate of WA is faster for finer particles due to their higher surface area to volume ratio. Since columnar grains are more likely to form in materials produced by directional solidification, where the solidification front moves in a single direction, promoting the growth of elongated columnar grains along the direction of solidification. Hence in laser powder bed fusion process, the solidification front moves vertically upward from the build plate as each layer is melted and solidified. So columnar grain growth would be more likely to occur in WA powders due to faster solidification rate, which could promote the formation and growth of elongated grains.

Figs. 5(e, f) illustrate that the fraction of ferritic zones in the WA sample was greater than in the GA sample. The extensive ferritic regions formed around the melt pool border of WA samples resulted from the heterogeneous nucleation of ferritic grains on the coarse inclusions that were pushed toward the melt pool boundaries. Pole figures (PFs) in **Figs. 5(g, h)** show that columnar austenitic grains aligned vertically along the BD, resulting in a strong crystallographic texture in the <001> direction. The higher texture index of the PFs suggests more elongated grains and anisotropic properties in the WA sample. Kernel Average Misorientation (KAM) distribution maps were utilized to compare the local grain misorientation and density of geometrically necessary dislocations (GNDs) in GA and WA samples (**Figs. 6(a, b)**). During the additive manufacturing (AM) process, remelting/reheating of successive layers leads to an inhomogeneous spreading of dislocations caused by the continuous reorientation of grain boundaries **[48]**. The KAM map reflects the degree of misorientation between a specific point (kernel) of a grain and its surrounding points (usually below 5°), with a higher KAM value indicating higher

dislocation motion and localized lattice distortion [49]. Strain accumulation primarily occurs near grain boundaries, and the grain interiors are often stress-free, particularly in the GA sample [50]. The stress localization around the grain boundaries compels adjacent grains to increase their misorientation and maintain continuity between them, resulting in the formation of more geometrically necessary dislocations (GNDs) around the grain boundaries [51]. According to the strain gradient theory, a Geometrically Necessary Dislocation (GND) array is defined for simple cylinder torsion. It is assumed that the cylinder contains a series of twist subgrain boundaries, each of which holds two perpendicular arrays of screw dislocations. To calculate the GNDs, the following equation can be employed:

$$\rho_{GND} = \frac{2\theta}{\mu b} \tag{3}$$

where ρ_{GND} is the GND density at the point of analysis, θ represents the local misorientation angle, μ is the unit length of the point ($\mu = 2x$, where x is the step size used when taking the EBSD images), and b is the Burger's vector [52]. The WA samples exhibited more inclusions enriched with Si, Cr, and Mn, which contributed to the promotion of GNDs being generated around their interface with the austenitic matrix. The proliferation of dislocations is correlated with the misorientation distribution in grains, and the extent of residual stress and plastic deformation in a single grain can be quantified by analyzing the grain orientation spread (GOS) [53]. The GOS pattern indicates the average deviation in orientation of each pixel of grain from the average orientation of that grain [54]. So higher GOS values indicate greater distortion in a grain, while approaching the recrystallized state appears with a lower GOS value. **Figs. 6(c)** and **6(d)** present the GOS maps of the GA and WA samples, respectively. The results demonstrate that faster solidification in the WA sample resulted in higher residual strain and a greater GOS value [55]. The high concentration of residual strain on grain boundaries (GBs) activated slip systems around the interface and led to the generation of more GNDs [56]. Regions with higher KAM, such as hatching distances where adjacent laser tracks overlapped, exhibited higher GOS values and an increased presence of low-angle boundaries (**Figs. 6(e, f)**).

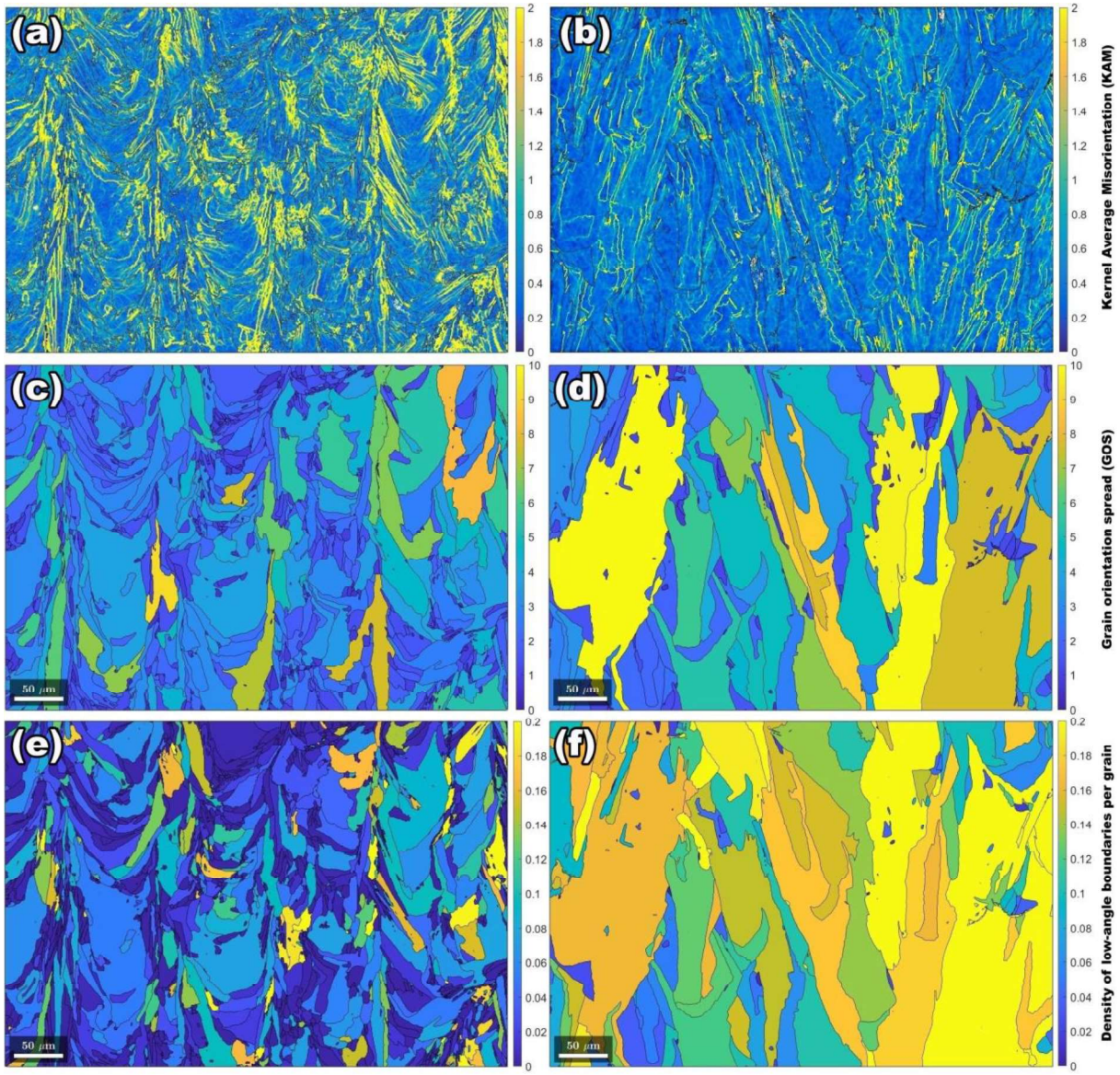

Fig. 6. Kernel average Misorientation (KAM) map (a, b), grain orientation spread (GOS) map (c, d) and distribution of low angle grain boundaries (LAGBs) inside the grains (e, f) in GA and WA samples, respectively.

Fig. 7(a, b) displays the tilt (blue) and tilt/twist (red) grain boundaries. Often tilt boundaries forms due to the misalignment of the crystal lattice between adjacent grains, while twist boundaries occur when the lattice is rotated around a common axis. The formation of tilt and twist boundaries can be influenced by the preferred crystallographic orientation of the grains, which can be affected by the cooling rate during solidification. On the other hand, twist boundaries occur when grains rotate about an axis that is perpendicular to their growth direction, leading to a misalignment in the lattice that results

in a twist boundary. The reason for the higher proportion of tilt boundaries in the WA sample is that the higher cooling rate during solidification led to higher likelihood of elongated neighboring grains having a small misorientation angle. In WA sample, the high cooling rate during solidification can promote the formation of tilt boundaries due to the restriction of grain growth. As the temperature of the melt decreases rapidly, the rate of crystal growth reduces, and grains have less time to grow to their maximum size. As a result, smaller grains with a higher number of low-angle boundaries are formed. These low-angle boundaries are mainly of the tilt type, which is characterized by a small misorientation angle between adjacent grains. Additionally, the presence of inclusions and impurities in the WA powders can also promote the formation of tilt boundaries. In contrast, GA powders typically have a slower cooling rate and a more equiaxed microstructure, which favors the formation of twist boundaries. The twisting in GA sample can occur because the misorientation angle is large enough to accommodate the lattice misfit between the grains. In regions like hatching distance where the grains have a similar crystallographic orientation and the boundary is not affected by other factors, tilted boundaries typically had a lower misorientation angle than twisted boundaries. That's because tilted grain boundaries are characterized by a smaller angular difference in crystal orientation between adjacent grains, while twisted grain boundaries involve a combination of tilt and rotational misalignment that results in a larger misorientation angle. The misorientation angle of the grain boundaries and associated distribution histogram are presented in **Fig. 7(c, d)** and **Fig. 7(e, f)**, respectively. The misorientation angle of a grain boundary refers to the angular difference in crystal orientation between two adjacent grains, resulting from the lattice mismatch at the grain interface. This misorientation angle is closely related to the Kernel Average Misorientation (KAM) value, which serves as an indicator of local crystallographic disorder. As the misorientation angle between neighboring grains increases, the KAM value also rises, reflecting a higher level of crystallographic disorder in the vicinity. However, the relationship between the magnitude of strain gradients and the misorientation angle of the grain boundary is not always straightforward, particularly in high-angle grain boundaries. The strain accumulation in such boundaries is influenced by the slip continuity across the boundary, which, in turn, depends on the alignment of the activated slip systems between the neighboring grains. When the slip plane and slip direction align closely, and the angle between the slip planes at the boundary is small, dislocation slip transmission becomes

more likely [57]. Consequently, in certain cases of misoriented grain boundaries where there is a good alignment of slip systems, the KAM value may be low, even if the misorientation angle of the grain boundary is large.

The density of geometrically necessary dislocations (GNDs) directly relates to the degree of crystallographic disorder within a material, and regions with higher KAM values generally exhibit higher GND densities. The misorientation angle of grain boundaries can also influence the GND density, as higher misorientation angles can lead to greater lattice strain and stress concentrations at the grain boundary. Consequently, regions with high misorientation angles between adjacent grains tend to have more GNDs compared to regions with lower misorientation angles. The density of GNDs is proportional to the misorientation angle of the grain boundaries. In the WA sample, the higher misorientation angles between adjacent grains necessitate more dislocations to accommodate the lattice curvature, resulting in a higher GND density [58, 59]. Furthermore, the measurement of misorientation angles in additive manufacturing (AM) fabricated samples indicates a larger fraction of low-angle grain boundaries (LAGBs) ($2° \leq \theta \leq 15°$) in the WA sample, while the GA sample shows more high-angle grain boundaries (HAGBs) ($15° < \theta$). It is also evident that elongated grains in both GA and WA samples exhibit the minimum misorientation with their adjacent grains. In the GA sample, such grains are primarily formed in the hatch zone, whereas the WA sample shows coarse elongated grains with the least deviation from the building direction, exhibiting the lowest misorientation with neighboring grains.

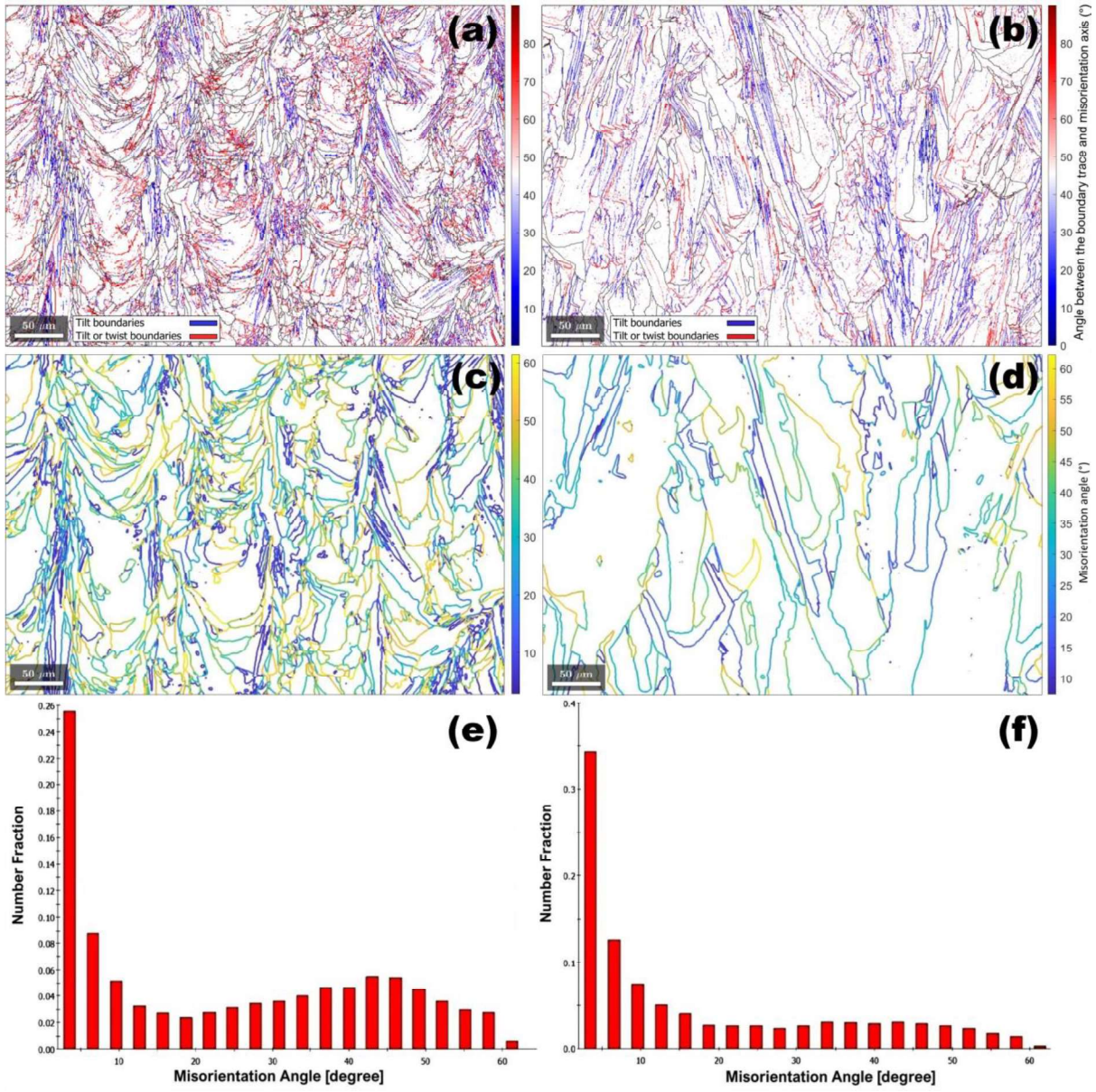

Fig. 7. Visualized misorientation angle of the grain boundaries (a, b), and the associated graph showing the distribution of misorientation angle of the grains (c, d) in WA and GA samples.

SEM micrographs in **Figs. 8 (a, b)** reveal the presence of residual δ-ferrite on the cellular structure of both GA (**Fig. 8(a)**) and WA (**Fig. 8(b)**) samples due to rapid solidification during AM. The WA sample, with a lower average particle size of powder and more penetration depth of the laser beam, exhibited more cohesive bonding at the melt pool boundaries (**Figs. 8(c, d)**). This can be attributed to the larger surface area of the WA powder, which allows for more efficient energy absorption and melting, and the irregular shape of its particles, which promotes better packing density and interlocking of particles

resulting in stronger bonding between layers. During printing, successive laser scans overlap each other, creating a continuous track in hatch space. This overlap leads to the establishment of a steady-state temperature gradient, which can influence the formation of tilt boundaries. Because, preferential growth direction of adjacent grains can contribute to the formation of tilted grain boundaries when the relative position of the grain boundary plane aligns with the rotation axis, leading to a misalignment of the crystal lattice. Factors such as local cooling rates, thermal gradients, and solute segregation influence the solidification process in the melt pools, where the laser power is concentrated, and the highest temperature is attained. The differences in crystal growth rates caused by these factors result in twisted grains, altering the plane where the crystal meets the melt pool, and leading to complex three-dimensional grain structures.

Comparing the cell size in WA and GA samples (**Figs. 8(e, f)**) showed smaller and more delicate cells in the WA sample due to its higher under-cooling and solidification rate. A similar observation has been reported for fabricated samples using LPBF and electron beam melting (EBM) additive manufacturing methods, where a lower solidification rate due to pre- and post-sintering of the deposited layers by EBM resulted in a coarser cellular structure with thicker cell walls **[60]**. The formation of finer cells results in a larger density of cell walls, which are essentially sub-grain boundaries consisting of twisted dislocations. This finding is consistent with the XRD and EBSD outputs that showed a higher dislocation density and GNDs in the WA sample, respectively.

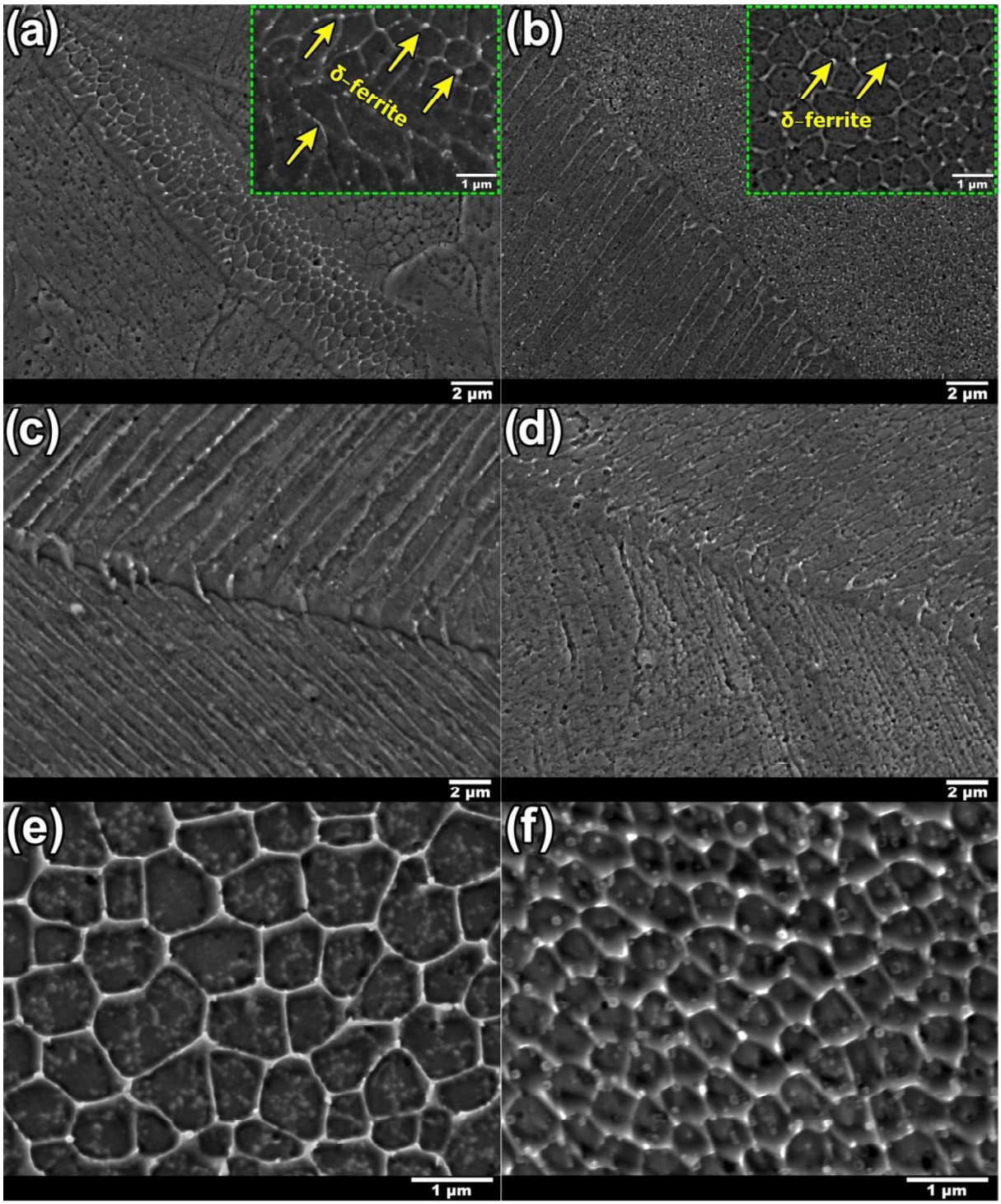

Fig. 8. SEM micrographs showing the cellular structures in GA (a, c and e), and WA (b, d, and f) samples.

4. Mechanical properties

The mechanical properties of both WA and GA samples were evaluated and the results are presented in **Fig. 9**. The stress-strain curves in **Fig. 9(a)** clearly indicate the superior tensile strength of the WA sample. The data extracted from the stress-strain curves reveals that the WA sample exhibited higher ultimate tensile strength (728 MPa vs 602 MPa), yield strength (580 MPa vs 503 MPa), toughness (underneath area of the stress-strain curve) (215 J/m3 vs 145 J/m3), and elongation (31.8% vs 25.2%) compared to the GA sample. It has been reported in the literature that the processability and circulation in the molten pool of GA track are more suitable for coarse particles, while smaller size range powders in WA feedstocks provide better performance **[61]**. The stereo and SEM micrographs of the fracture surfaces provided in the results show that the WA sample exhibits finer dimples which is consistent with the higher strength and finer cellular structure in WA sample.

The work hardening rate micrographs of **Fig. 9(b)** indicate that dislocations glide easily at stage I of deformation for both samples. The primary difference between the WA and GA samples is in transition stage II, where hardening attenuates at a lower rate in the WA sample. The behavior of the material in the second stage is the result of a trade-off between hardening and softening phenomena such as partial glide of dislocations, generation of new geometrically necessary dislocations, and annihilation of dislocations through dynamic recovery. The presence of dislocation tangles can hinder the movement of free dislocations and restrict the formation of new dislocations. The stress field generated around these dislocation clogs creates a pinning effect that ultimately boosts the tensile strength of the material **[62]**. The higher work hardening rate in the WA sample in comparison to the GA sample can be attributed to various factors. As previously mentioned, the WA sample had a greater number of tilted grain boundaries, which are linked to a higher work hardening rate compared to twist grain boundaries. This is because tilted grain boundaries obstruct the movement of dislocations, which are the primary carriers of plastic deformation in metals. The higher density of tilt grain boundaries is more effective at hindering dislocation movement, leading to a higher work hardening rate. Additionally, the WA sample contained more inclusions compared to the GA sample. These inclusions can act as obstacles to dislocation motion, leading to pile-ups and forest dislocations, which further contribute to strain hardening. Furthermore, inclusions can create local stress fields in the printed parts,

affecting the distribution and movement of dislocations and leading to the formation of deformation structures such as dislocation walls and cell structures. At the interface between the inclusion and the surrounding matrix, there is typically a region of high stress gradient due to the difference in elastic properties between the inclusion and the matrix. This can lead to the formation of a plastic deformation zone around the inclusion where local stresses exceed the yield strength of the material. The local stress field experienced by a dislocation encountering an inclusion can increase the energy required for its motion. The strength of the resistance to dislocation motion is proportional to the strength of the local stress field, which depends on the size, shape, and orientation of the inclusion and the surrounding crystal lattice. As depicted in **Fig. 9(c)**, the GA sample exhibited a more uniform distribution and a slightly higher average microhardness compared to the WA sample (237 vs. 229, respectively). The fluctuation in the hardness values in the WA sample can be attributed to a higher percentage of defects and inclusions, which can act as hard and brittle phases **[36]**.

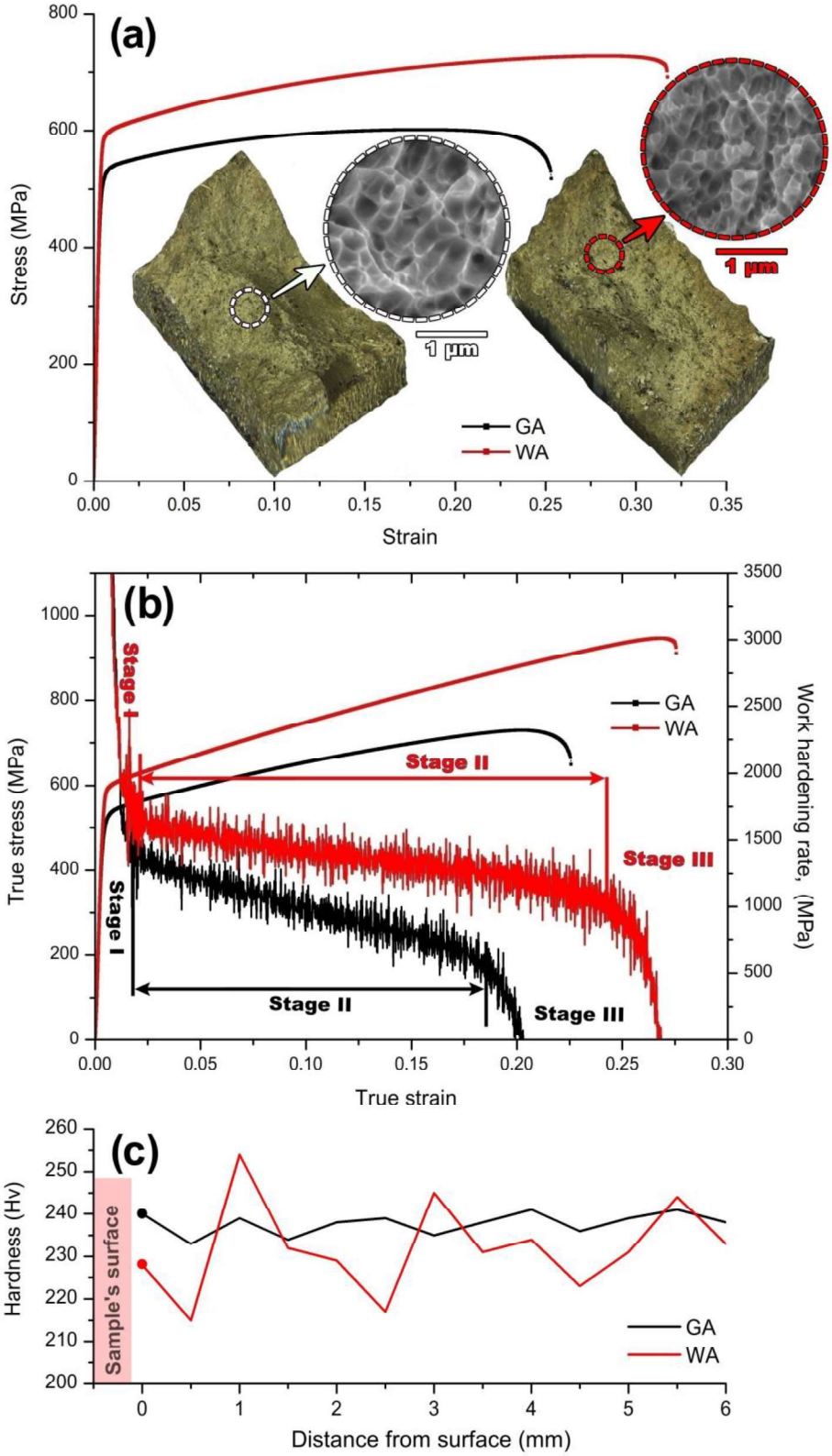

Fig. 9. Engineering stress-strain curves, stereo macrographs, and SEM micrographs of the fracture surfaces (a), true stress-true strain curves and variation of work hardening rate (b), and variation of the Vickers microhardness (c), in GA and WA samples.

The SEM analysis revealed the presence of spherical (**Fig. 10(a)**) or irregularly shaped (**Fig. 10(b)**) inclusions at the bottom of a few dimples on the fracture surface of the WA specimen. Furthermore, the corresponding elemental distribution map of the WA sample (**Figs. 10(c)**) confirmed the presence of multiple fine inclusions containing Si, Cr, and Mn. The WA powder used in the production process had a high residual oxygen content, leading to its reaction with Si, Mn, and Cr and the formation of submicron oxides **[63]**. The formation of these particulates can directly affect the mechanical properties **[64]**. Kong et al. have illustrated that demonstrated that the formation of nano-twins around such inclusions in additively manufactured SS316L samples could improve the material's resistance against crack propagation **[65]**. However, their coarsening during annealing could have the opposite effect and degrade the mechanical properties **[66]**.

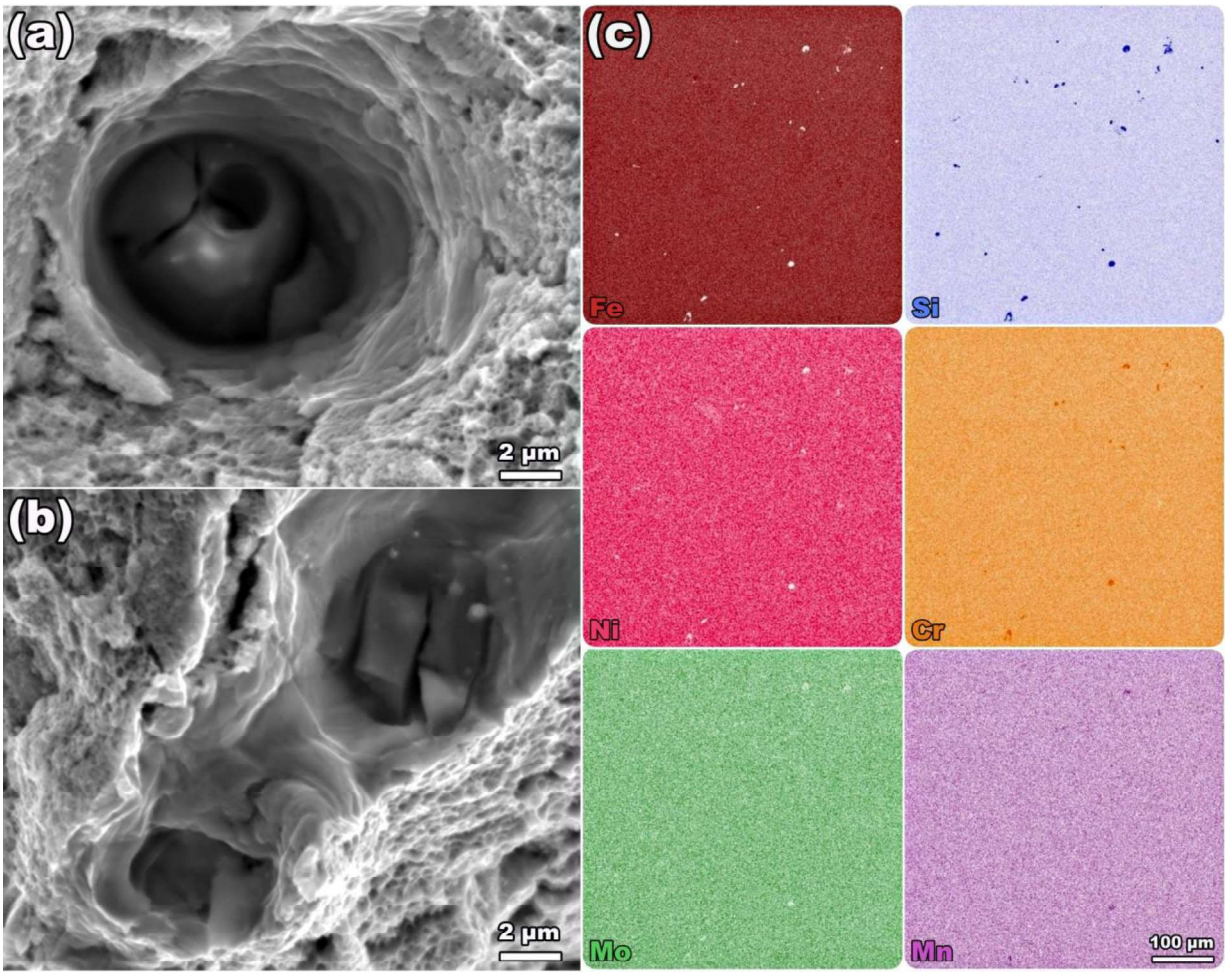

Fig. 10. SEM micrographs of the inclusions formed in WA sample (a, b) and the elemental distribution map acquired from the WA sample (c).

The 3D surface topology of the GA and WA samples is depicted in **Fig. 11**. As observed, the side surface of the WA sample appears to be relatively more uniform and less rough compared to the GA sample. The surface profile of the WA sample has a maximum peak height of about 16.6 µm, which is much lower than the peak height of about 46.2 µm for the GA sample. This indicates a smoother surface for the WA specimen. The irregular shape of WA powder particles can lead to increased surface area, which results in higher laser absorption during the LPBF process. Additionally, the finer particle size of WA powder can result in higher packing density of the powder bed and contribute to higher laser absorption as the smaller particles have a larger surface area-to-volume ratio, allowing for more efficient energy transfer from the laser to the powder particles. Higher laser absorption led to more efficient melting of the powder particles, resulting in a smoother surface finish and lower surface roughness in the WA sample.

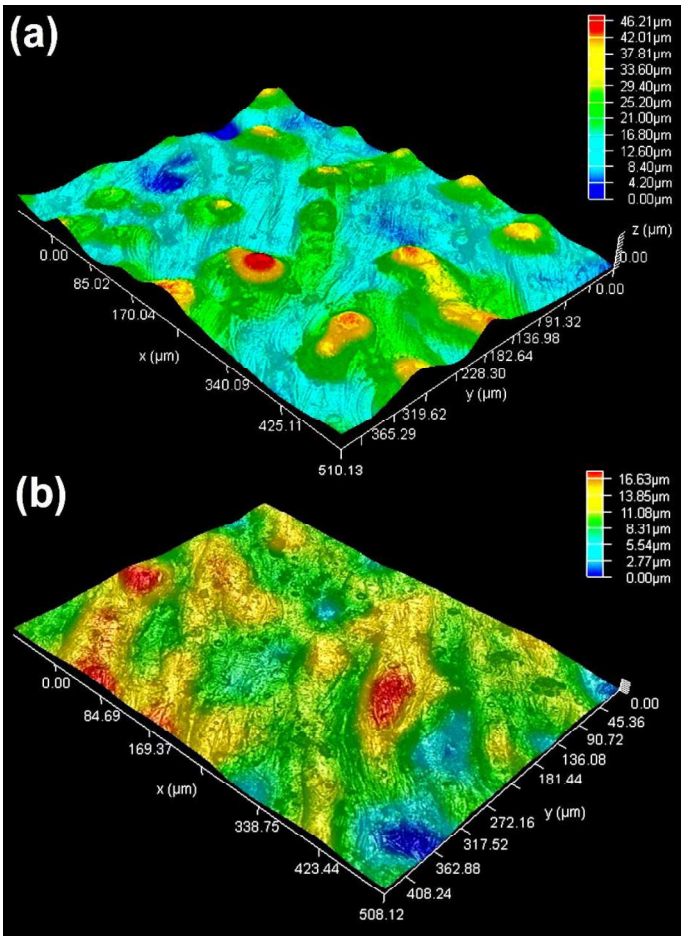

Fig. 11. Illustration of 3D surface roughness of the GA (a) and WA (b) samples.

5. *Corrosion behaviour*

The electrochemical behavior of the samples was examined using CPP and EIS measurements. **Fig. 12** presents the CPP curves of both the GA and WA samples. Initially, the specimens showed similar open circuit potential (OCP) values. However, the cathodic branches of the curves exhibited slight differences for the GA and WA samples. Generally, in the cathodic branch, the electrode surface undergoes oxygen reduction, and the kinetics are determined by the diffusion rate of oxygen from the solution. In contrast, distinct differences were observed in the anodic portion of the curve. The GA samples displayed higher current density values in the anodic part, which was also reflected in the corrosion current density (icorr.) calculated through Tafel interpolation.

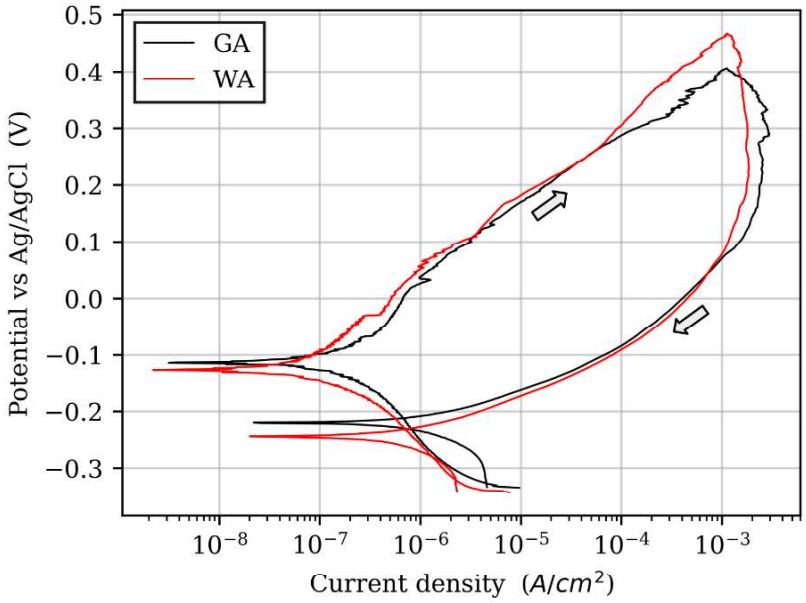

Fig. 12. Cyclic potentiodynamic polarization (CPP) curves of the GA and WA samples acquired in 3.5 wt% NaCl solution. Scan direction is indicated by arrows.

Table 3 reveals that the corrosion current density ($i_{corr.}$), which is proportional to the corrosion rate, was three times higher for the GA sample compared to the WA sample. The higher corrosion potential ($E_{corr.}$) of the GA sample is consistent with the OCP values, indicating a slightly nobler behavior of the GA sample. The lower corrosion rate observed in the WA sample may be attributed to the higher residual stresses and dislocation densities in the WA sample which promotes the formation of a compact and continuous passive layer. This passive layer acts as a barrier, reducing the direct contact between the metal surface

and the corrosive environment. The uniformity and stability of the passive layer provide enhanced protection against aggressive ions and minimize the occurrence of localized corrosion sites.

Table. 3. Comparison of the most important parameters derived from CPP measurements for the GA and WA samples.

	OCP (mV vs Ag/AgCl)	E corr. (mV vs Ag/AgCl)	i corr. (A/cm^2)	E pass. (mV vs Ag/AgCl)
GA	-113.3 ± 20.6	-114.8 ± 6.4	$13.8 \cdot 10^{-8} \pm 7.98 \cdot 10^{-8}$	-242.0 ± 18.7
WA	-138.3 ± 24.0	-134.3 ± 29.6	$4.63 \cdot 10^{-8} \pm 2.64 \cdot 10^{-8}$	-249.0 ± 11.5

In the anodic branch of the curve, both samples displayed an active behavior that resulted in increasing current density with higher applied potentials. Additionally, the current peaks observed in the anodic branch could be attributed to metastable pitting. However, due to the lack of a passive region, it was difficult to identify the pitting potential, which is an important parameter to describe the behavior of stainless steels. After reaching the cycle vertex at a current density of 1 mA/cm2, the scan was reversed, and the current density values remained high over a wide range of potential, indicating the formation of stable pitting in this range of over-potential. Re-passivation occurred at applied potentials below the corrosion potential, which was about -242.0 mV for the GA sample and -249.0 mV for the WA sample.

The electrochemical behavior observed in the CPP curves was confirmed by the EIS measurements. As shown in **Fig. 13**, the WA sample exhibited a slightly more protective superficial oxide layer in the chloride solution. This is supported by a higher maximum value in the phase of the Bode diagrams, indicating better protection. The impedance modulus at low frequency was also higher for the WA sample, which suggests a more efficient protective layer and lower corrosion rate compared to the GA sample. The lower density of grain boundaries in the WA sample can contribute to its higher corrosion resistance. Grain boundaries are often sites for localized corrosion initiation, and having fewer grain boundaries in WA sample would result in lower intergranular corrosion. Tilted grain boundaries can also hinder dislocation motion, leading to more homogeneous deformation behavior, and hence a more uniform distribution of stresses and strains. This could also improve the corrosion resistance of WA sample by reducing the concentration of localized

stresses. The lattice distortion caused by higher KAM and GOS in WA sample could trap corrosive species and prevent them from diffusing deeper into the material. It would also create a self-passivating behavior, where a protective oxide layer forms on the surface, hindering further corrosion.

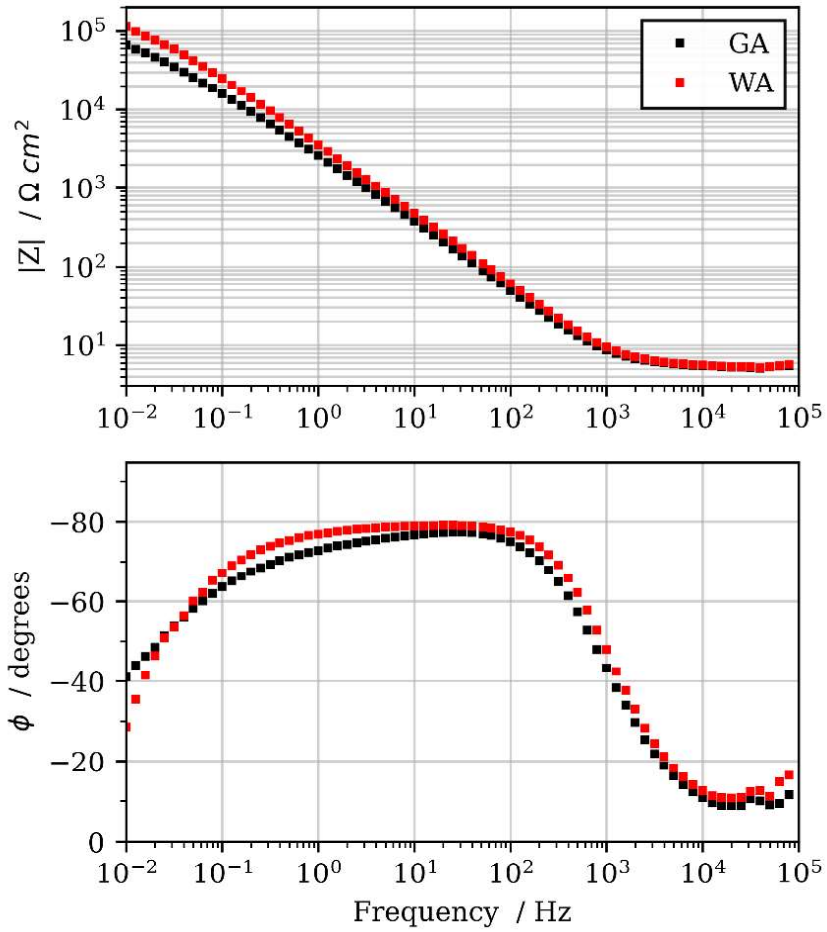

Fig. 13. Two representative EIS spectra reported as Bode diagrams acquired on the GA and WA samples in 3.5 wt.% NaCl solution.

The validity of the above observations was further confirmed by modeling the EIS spectra using equivalent electrical circuits (EEC). The EEC utilized in this study is shown in **Fig. 14** and includes the solution resistance (R_s), the resistance to charge transfer (R_{ct}), and the double layer capacitance (CPE_{dl}).

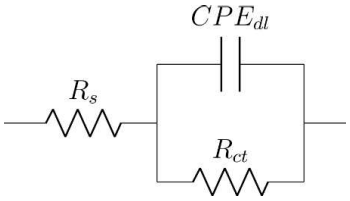

Fig. 14. Equivalent Electrical Circuit (EEC) used to model the impedance spectra.

To model time constant dispersion on the electrode surface, a Constant Phase Element (CPE) was utilized **[67]**. The solution resistance was obtained from the high-frequency impedance, where the phase approaches 0°, and was found to be constant for both samples, as expected. However, minor yet statistically significant variations were detected in the values of R_{ct} and CPE_{dl}, which are directly linked to the corrosion rate and double-layer capacitance non-faradaic processes, respectively (**Table 4**). Interestingly, the EEC fitting method revealed that both Rct and CPE_{dl} values were higher for the WA sample, indicating its superior corrosion resistance. Additionally, for both samples, the CPE parameter (n) approached unity, indicating a behavior that is comparable to a pure capacitor for this circuit element.

Table. 4. Comparison of the EEC elements values for the GA and WA samples.

	R_s ($\Omega \cdot cm^2$)	R_{ct} ($\Omega \cdot cm^2$)	CPE_{dl} ($s^n/(\Omega \cdot cm^2)$)	n
GA	5.5 ± 0.2	$1.24 \cdot 10^5 \pm 0.78 \cdot 10^5$	$8.5 \cdot 10^{-5} \pm 8.0 \cdot 10^{-6}$	0.86 ± 0.01
WA	5.5 ± 0.2	$1.15 \cdot 10^5 \pm 0.16 \cdot 10^5$	$6.23 \cdot 10^{-5} \pm 1.2 \cdot 10^{-5}$	0.88 ± 0.01

The SEM images shown in **Fig. 15** provide a visual representation of the surface of the GA and WA samples following the potentiodynamic polarization test. The GA sample was found to be more susceptible to aggressive ions in the corrosive media, while the WA sample exhibited less severe pitting corrosion despite having a higher content of inclusions. This is likely because the WA sample had a negligible Mn content, which reduced the likelihood of MnS inclusion formation. Moreover, the absence of Cr depletion in the vicinity of MnS inclusions further would enhance the material's corrosion resistance.

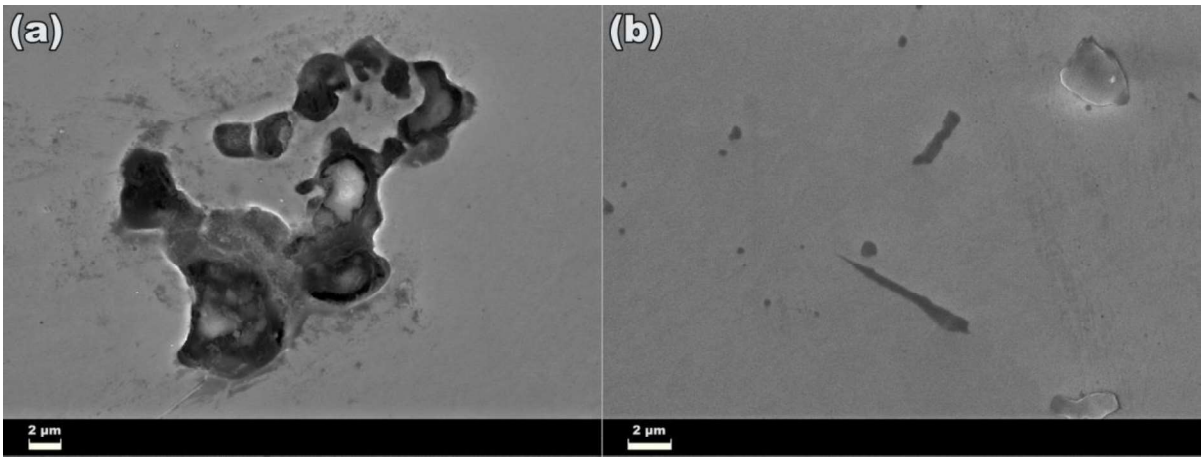

Fig. 15. SEM images from the side surface of the GA (a) and WA (b) samples after the CPP test.

Formation of inclusions in WA sample can make a more uniform and stable passive layer by promoting the accumulation of dislocations and strain hardening of the surrounding matrix. This stress field can result in the creation of a denser and more uniform passive layer as an effective barrier against the penetration of chloride ions and other aggressive species that can cause corrosion. Although, inclusions can act as preferential sites for the nucleation of pitting corrosion. But the presence of a more uniform passive layer around the inclusions can prevent the formation and propagation of pits, leading to an increase in the corrosion resistance of the WA sample. These inclusions would also contribute in trapping the immobilize corrosive species at the surface of the printed parts, reducing their ability to react with the underlying austenitic matrix and form localized corrosion sites.

Concluding remarks

In this study, GA and WA powders of SS316L were used as the initial feedstock for LPBF additive manufacturing, with the WA powder having a finer average size. The microstructure and mechanical properties of the printed parts are compared together. The main findings of this research can be summarized as follows:

- Higher oxygen content in the WA powder, combined with Cr, Mn, and Si, formed multiple inclusion that resulted in non-uniform hardness distribution in the WA printed sample, while it had a more even distribution in the GA sample.
- The higher laser absorption of WA compared to GA powder resulted in faster solidification of the deposited layers as well as higher thermal stress and wider ferritic regions in the WA sample.
- According to microstructural characterization, the WA specimen featured higher lattice distortion, evidenced by higher GOS, LAGBs, and dislocation density, as well as finer cellular structure. In fact, to preserve the integrity of the material during rapid solidification, the lattice generated more GNDs around the elongated grains. These elongated grains had tilted boundaries with the lowest misorientation with the adjacent grains.
- Due to the higher laser beam penetration depth and cooling rate, the WA sample had more columnar grains and a stronger texture along the BD.
- The results of the tensile test revealed that the WA sample shows higher UTS, YS, El%, and toughness (728 MPa, 580 MPa, 31.8%, and 215 J/m^3 respectively) than the GA sample (602 MPa, 503 MPa, 25.2%, 145 J/m^3 respectively). Also, it exhibited a higher work hardening rate and finer dimples on its fracture surface compared to GA one.
- Comparison of the CPP and EIS curves with the SEM images of the corrosion products revealed that, although multiple inclusions were formed, the presence of a higher density of tilted grain boundaries and dislocations resulted in a more stable passive layer on the surface of the WA sample that led to a higher resistance against corrosion in chloride-containing corrosive media.

Acknowledgement

The authors appreciate the integrated additive manufacturing (IAM) center of Politecnico di Torino for printing the samples. The first author acknowledges recommendations from Prof. E. Ghasemali from Jönköping University.

References

[1] M.R. Jandaghi, H. Pouraliakbar, V. Fallah, E. Ghassemali, A. Saboori, M. Pavese, Additive manufacturing of nano-oxide decorated AlSi10Mg composites: A comparative study on Gd2O3 and Er2O3 additions, Materials Characterization, (2022) 112206.
[2] A. Averardi, C. Cola, S.E. Zeltmann, N. Gupta, Effect of particle size distribution on the packing of powder beds: A critical discussion relevant to additive manufacturing, Materials Today Communications, 24 (2020) 100964.
[3] M.R. Jandaghi, A. Aversa, D. Manfredi, F. Calignano, L. Lavagna, M. Pavese, In situ alloying of AlSi10Mg-5 wt% Ni through laser powder bed fusion and subsequent heat treatment, Journal of Alloys and Compounds, 904 (2022) 164081.
[4] H. Qin, V. Fallah, Q. Dong, M. Brochu, M.R. Daymond, M. Gallerneault, Solidification pattern, microstructure and texture development in Laser Powder Bed Fusion (LPBF) of Al10SiMg alloy, Materials Characterization, 145 (2018) 29-38.
[5] T.F. Murphy, C.T. Schade, Measurement of powder characteristics and quality for additive manufacturing in aerospace alloys, Additive Manufacturing for the Aerospace Industry, (2019) 99-142.
[6] M. Boisvert, D. Christopherson, P. Beaulieu, G. L'Espérance, Treatment of ferrous melts for the improvement of the sphericity of water atomized powders, Materials & Design, 116 (2017) 644-655.
[7] P. Wang, A. Salandari-Rabori, Q. Dong, V. Fallah, Effect of input powder attributes on optimized processing and as-built tensile properties in laser powder bed fusion of AlSi10Mg alloy, Journal of Manufacturing Processes, 64 (2021) 633-647.
[8] S. Zhang, Q.S. Wei, G.K. Lin, X. Zhao, Y.S. Shi, Effects of powder characteristics on selective laser melting of 316L stainless steel powder, Advanced Materials Research, Trans Tech Publ, 2011, pp. 3664-3667.
[9] K. Kassym, A. Perveen, Atomization processes of metal powders for 3D printing, Materials today: proceedings, 26 (2020) 1727-1733.
[10] T. Fedina, J. Sundqvist, J. Powell, A.F. Kaplan, A comparative study of water and gas atomized low alloy steel powders for additive manufacturing, Additive Manufacturing, 36 (2020) 101675.
[11] M. Abdelwahed, R. Casati, A. Larsson, S. Petrella, S. Bengtsson, M. Vedani, On the Recycling of Water Atomized Powder and the Effects on Properties of L-PBF Processed 4130 Low-Alloy Steel, Materials, 15 (2022) 336.
[12] J.P. Kruth, P. Mercelis, J. Van Vaerenbergh, L. Froyen, M. Rombouts, Binding mechanisms in selective laser sintering and selective laser melting, Rapid prototyping journal, (2005).
[13] M. Elahinia, N.S. Moghaddam, M.T. Andani, A. Amerinatanzi, B.A. Bimber, R.F. Hamilton, Fabrication of NiTi through additive manufacturing: A review, Progress in Materials Science, 83 (2016) 630-663.
[14] E. Vasquez, P.-F. Giroux, F. Lomello, M. Nussbaum, H. Maskrot, F. Schuster, P. Castany, Effect of powder characteristics on production of oxide dispersion strengthened Fe14Cr steel by laser powder bed fusion, Powder Technology, 360 (2020) 998-1005.
[15] E. Olakanmi, Selective laser sintering/melting (SLS/SLM) of pure Al, Al–Mg, and Al–Si powders: Effect of processing conditions and powder properties, Journal of Materials Processing Technology, 213 (2013) 1387-1405.

[16] A. Demir, L. Monguzzi, B. Previtali, Selective laser melting of pure Zn with high density for biodegradable implant manufacturing, Addit. Manuf. 15 (2017) 20–28.
[17] P. Moghimian, T. Poirié, M. Habibnejad-Korayem, J.A. Zavala, J. Kroeger, F. Marion, F. Larouche, Metal powders in additive manufacturing: A review on reusability and recyclability of common titanium, nickel and aluminum alloys, Additive Manufacturing, 43 (2021) 102017.
[18] A. Mostafaei, J. Toman, E.L. Stevens, E.T. Hughes, Y.L. Krimer, M. Chmielus, Microstructural evolution and mechanical properties of differently heat-treated binder jet printed samples from gas- and water-atomized alloy 625 powders, Acta Materialia, 124 (2017) 280-289.
[19] R. Engeli, T. Etter, S. Hövel, K. Wegener, Processability of different IN738LC powder batches by selective laser melting, Journal of Materials Processing Technology, 229 (2016) 484-491.
[20] A.O. Moghaddam, N.A. Shaburova, M.N. Samodurova, A. Abdollahzadeh, E.A. Trofimov, Additive manufacturing of high entropy alloys: A practical review, Journal of Materials Science & Technology, 77 (2021) 131-162.
[21] D. Herzog, V. Seyda, E. Wycisk, C. Emmelmann, Additive manufacturing of metals, Acta Materialia, 117 (2016) 371-392.
[22] J. SCHRAGE, J.H. SCHLEIFENBAUM, INFLUENCE OF POWDER APPLICATION PARAMETERS ON POWDER BED PROPERTIES AND ON PRODUCTIVITY OF LASER POWDER BED FUSION (L-PBF).
[23] S. Chikosha, L.C. Tshabalala, H. Bissett, M. Lesufi, N.K. Mnguni, T.M. Motsai, T. Manama, S. Hoosain, Spheroidisation of Stainless Steel Powder for Additive Manufacturing, Metals, 11 (2021) 1081.
[24] J.-Y. Park, K.B. Park, J.-W. Kang, H.G. Kim, N.-M. Hwang, H.-K. Park, Spheroidization behavior of water-atomized 316 stainless steel powder by inductively-coupled thermal plasma, Materials Today Communications, 25 (2020) 101488.
[25] S. Mirzababaei, S. Pasebani, A review on binder jet additive manufacturing of 316L stainless steel, Journal of Manufacturing and Materials Processing, 3 (2019) 82.
[26] S. Pasebani, M. Ghayoor, S. Badwe, H. Irrinki, S.V. Atre, Effects of atomizing media and post processing on mechanical properties of 17-4 PH stainless steel manufactured via selective laser melting, Additive Manufacturing, 22 (2018) 127-137.
[27] L. Haferkamp, A. Spierings, K. Wegener, K. Riener, S. Ziegelmeier, G. Leichtfried, The Influence of Particle Shape, Powder Flowability, and Powder Layer Density on Part Density in Laser Powder Bed Fusion, Metals, 11 (2021).
[28] S. Cacace, Q. Semeraro, Influence of the atomization medium on the properties of stainless steel SLM parts, Additive Manufacturing, 36 (2020) 101509.
[29] I. Rishmawi, A. Rogalsky, M. Vlasea, A. Molavi-Kakhki, Comparison of the master sinter curves of water-and gas-atomized AISI 4340 low-alloy steel in binder jetting additive manufacturing, Additive Manufacturing, 48 (2021) 102381.
[30] N. Tepylo, X. Huang, P.C. Patnaik, Laser-based additive manufacturing technologies for aerospace applications, Advanced Engineering Materials, 21 (2019) 1900617.
[31] U.S. Bertoli, G. Guss, S. Wu, M.J. Matthews, J.M. Schoenung, In-situ characterization of laser-powder interaction and cooling rates through high-speed imaging of powder bed fusion additive manufacturing, Materials & Design, 135 (2017) 385-396.
[32] J.S. Weaver, J. Whiting, V. Tondare, C. Beauchamp, M. Peltz, J. Tarr, T.Q. Phan, M.A. Donmez, The effects of particle size distribution on the rheological properties of the powder and the mechanical properties of additively manufactured 17-4 PH stainless steel, Additive Manufacturing, 39 (2021) 101851.
[33] H. Irrinki, J.S.D. Jangam, S. Pasebani, S. Badwe, J. Stitzel, K. Kate, O. Gulsoy, S.V. Atre, Effects of particle characteristics on the microstructure and mechanical properties of 17-4 PH stainless steel fabricated by laser-powder bed fusion, Powder Technology, 331 (2018) 192-203.
[34] M. Jandaghi, A. Saboori, L. Iuliano, M. Pavese, On the effect of rapid annealing on the microstructure and mechanical behavior of additively manufactured stainless steel by Laser Powder Bed Fusion, Materials Science and Engineering: A, 828 (2021) 142109.

[35] M.R. Jandaghi, H. Pouraliakbar, S.H. Shim, V. Fallah, S.I. Hong, M. Pavese, In-situ alloying of stainless steel 316L by co-inoculation of Ti and Mn using LPBF additive manufacturing: Microstructural evolution and mechanical properties, Materials Science and Engineering: A, 857 (2022) 144114.
[36] S. Hoeges, A. Zwiren, C. Schade, Additive manufacturing using water atomized steel powders, Metal Powder Report, 72 (2017) 111-117.
[37] A.J. Pinkerton, L. Li, Direct additive laser manufacturing using gas- and water-atomised H13 tool steel powders, The International Journal of Advanced Manufacturing Technology, 25 (2005) 471-479.
[38] T. Talako, A. Letsko, Modern Tendencies in Production of Metal Powders for Additive Manufacturing, (2017) 95-102.
[39] M. Abdelwahed, S. Bengtsson, R. Casati, A. Larsson, S. Petrella, M. Vedani, Effect of water atomization on properties of type 4130 steel processed by L-PBF, Materials & Design, 210 (2021) 110085.
[40] Y. Hedberg, O. Karlsson, P. Szakalos, I.O. Wallinder, Ultrafine 316L stainless steel particles with frozen-in magnetic structures characterized by means of electron backscattered diffraction, Materials Letters, 65 (2011) 2089-2092.
[41] J. Wanni, A. Colak, A. Achuthan, Subgrain microstructural features in directed energy deposited stainless steel 316L: The influence of morphology on mechanical properties, Materials Science and Engineering: A, 880 (2023) 145215.
[42] M. Ziętala, T. Durejko, M. Polański, I. Kunce, T. Płociński, W. Zieliński, M. Łazińska, W. Stępniowski, T. Czujko, K.J. Kurzydłowski, Z. Bojar, The microstructure, mechanical properties and corrosion resistance of 316L stainless steel fabricated using laser engineered net shaping, Materials Science and Engineering: A, 677 (2016) 1-10.
[43] M. Ghayoor, S. Badwe, H. Irrinki, S. Atre, S. Pasebani, Water Atomized 17-4 PH Stainless Steel Powder as a Cheaper Alternative Powder Feedstock for Selective Laser Melting, Materials Science Forum, 941 (2018) 698-703.
[44] J. Yu, M. Rombouts, G. Maes, Cracking behavior and mechanical properties of austenitic stainless steel parts produced by laser metal deposition, Materials & Design, 45 (2013) 228-235.
[45] J.H. Tan, W.L.E. Wong, K.W. Dalgarno, An overview of powder granulometry on feedstock and part performance in the selective laser melting process, Additive Manufacturing, 18 (2017) 228-255.
[46] T.F. Murphy, C.T. Schade, 6 - Measurement of powder characteristics and quality for additive manufacturing in aerospace alloys, in: F. Froes, R. Boyer (Eds.) Additive Manufacturing for the Aerospace Industry, Elsevier, 2019, pp. 99-142.
[47] A. Pinkerton, L. Li, Process characteristics and effects of gas- and water-atomized stainless steel powders in laser-based rapid tooling, Journal of Laser Applications, 15 (2003) 172-178.
[48] M. Godec, S. Zaefferer, B. Podgornik, M. Šinko, E. Tchernychova, Quantitative multiscale correlative microstructure analysis of additive manufacturing of stainless steel 316L processed by selective laser melting, Materials Characterization, 160 (2020) 110074.
[49] N. Sridharan, M. Gussev, R. Seibert, C. Parish, M. Norfolk, K. Terrani, S.S. Babu, Rationalization of anisotropic mechanical properties of Al-6061 fabricated using ultrasonic additive manufacturing, Acta Materialia, 117 (2016) 228-237.
[50] V. Chaudhary, N.M. Sai Kiran Kumar Yadav, S.A. Mantri, S. Dasari, A. Jagetia, R.V. Ramanujan, R. Banerjee, Additive manufacturing of functionally graded Co–Fe and Ni–Fe magnetic materials, Journal of Alloys and Compounds, 823 (2020) 153817.
[51] D. Lin, L. Xu, H. Jing, Y. Han, L. Zhao, Y. Zhang, H. Li, A strong, ductile, high-entropy FeCoCrNi alloy with fine grains fabricated via additive manufacturing and a single cold deformation and annealing cycle, Additive Manufacturing, 36 (2020) 101591.
[52] S. Peng, S. Mooraj, R. Feng, L. Liu, J. Ren, Y. Liu, F. Kong, Z. Xiao, C. Zhu, P.K. Liaw, Additive manufacturing of three-dimensional (3D)-architected CoCrFeNiMn high-entropy alloy with great energy absorption, scripta materialia, 190 (2021) 46-51.

[53] N. Sridharan, P. Wolcott, M. Dapino, S.S. Babu, Microstructure and texture evolution in aluminum and commercially pure titanium dissimilar welds fabricated using ultrasonic additive manufacturing, Scripta Materialia, 117 (2016) 1-5.
[54] M.E.J. Perry, R.J. Griffiths, D. Garcia, J.M. Sietins, Y. Zhu, H.Z. Yu, Morphological and microstructural investigation of the non-planar interface formed in solid-state metal additive manufacturing by additive friction stir deposition, Additive Manufacturing, 35 (2020) 101293.
[55] P. Niu, R. Li, S. Zhu, M. Wang, C. Chen, T. Yuan, Hot cracking, crystal orientation and compressive strength of an equimolar CoCrFeMnNi high-entropy alloy printed by selective laser melting, Optics & Laser Technology, 127 (2020) 106147.
[56] N. Sridharan, M. Norfolk, S.S. Babu, Characterization of steel-Ta dissimilar metal builds made using very high power ultrasonic additive manufacturing (VHP-UAM), Metallurgical and Materials Transactions A, 47 (2016) 2517-2528.
[57] J. Luster, M. Morris, Compatibility of deformation in two-phase Ti-Al alloys: Dependence on microstructure and orientation relationships, Metallurgical and Materials Transactions A, 26 (1995) 1745-1756.
[58] E. Demir, D. Raabe, N. Zaafarani, S. Zaefferer, Investigation of the indentation size effect through the measurement of the geometrically necessary dislocations beneath small indents of different depths using EBSD tomography, Acta Materialia, 57 (2009) 559-569.
[59] P.J. Konijnenberg, S. Zaefferer, D. Raabe, Assessment of geometrically necessary dislocation levels derived by 3D EBSD, Acta Materialia, 99 (2015) 402-414.
[60] M. Pitchandi, A.K. V, P. Pi, V. Ramachandran, S. Manwatkar, S. Rao, N. Svs, D. Sivakumar, P. Narayanan, On the anisotropy in room-temperature mechanical properties of laser powder bed fusion processed Ti6Al4V-ELI alloy for aerospace applications, Journal of Materials Science, (2022).
[61] B. Hausnerova, B.N. Mukund, D. Sanetrnik, Rheological properties of gas and water atomized 17-4PH stainless steel MIM feedstocks: Effect of powder shape and size, Powder Technology, 312 (2017) 152-158.
[62] D.A. Hughes, N. Hansen, The microstructural origin of work hardening stages, Acta Materialia, 148 (2018) 374-383.
[63] D. Riabov, E. Hryha, M. Rashidi, S. Bengtsson, L. Nyborg, Effect of atomization on surface oxide composition in 316L stainless steel powders for additive manufacturing, Surface and Interface Analysis, 52 (2020) 694-706.
[64] Y. Zhang, F. Ensheng, W. Mo, Y. Lv, R. Ma, S. Ye, P. Yu, On the Microstructures and Fatigue Behaviors of 316L Stainless Steel Metal Injection Molded with Gas- and Water-Atomized Powders, Metals, 8 (2018) 893.
[65] D. Kong, C. Dong, X. Ni, Z. Liang, X. Li, In-situ observation of asymmetrical deformation around inclusion in a heterogeneous additively manufactured 316L stainless steel, Journal of Materials Science & Technology, 89 (2021) 133-140.
[66] Q. Chao, S. Thomas, N. Birbilis, P. Cizek, P.D. Hodgson, D. Fabijanic, The effect of post-processing heat treatment on the microstructure, residual stress and mechanical properties of selective laser melted 316L stainless steel, Materials Science and Engineering: A, 821 (2021) 141611.
[67] M.E. Orazem, B. Tribollet, Electrochemical impedance spectroscopy, New Jersey, (2008) 383-389.